EUROPEAN ORGANIZATION FOR NUCLEAR RESEARCH
CERN — BEAMS DEPARTMENT

CERN-BE-2009-030 BI

The LHC Synchrotron-Light Monitors

A.S. Fisher, A. Goldblatt, T. Lefèvre

CERN – Geneva, Switzerland

Abstract

Synchrotron-light telescopes will measure the profiles of the two LHC beams of protons or lead ions, and verify that the abort gap is clear. At collision energy (7 TeV), each telescope will image visible light from a superconducting dipole used to widen beam separation at the RF cavities. At injection (0.45 TeV), this source must be supplemented by a 2-period superconducting undulator 1 m from the dipole. An optical "trombone" delay line will provide the large shift in focus. We discuss the optical design, diffraction, depth of field, and the expected signals over the energy ramp, for emission from the centre and edge of the dipole and from the undulator.

Paper presented at DIPAC'09 Conference – 25-27 May 2009 /Basel-CH

Geneva, Switzerland
June, 2009

THE LHC SYNCHROTRON-LIGHT MONITORS

A.S. Fisher*, SLAC National Accelerator Laboratory, Menlo Park, CA 94025, USA
A. Goldblatt and T. Lefevre, CERN, Geneva, Switzerland

Abstract

Synchrotron-light telescopes will measure the profiles of the two LHC beams of protons or lead ions, and verify that the abort gap is clear. At collision energy (7 TeV), each telescope will image visible light from a superconducting dipole used to widen beam separation at the RF cavities. At injection (0.45 TeV), this source must be supplemented by a 2-period superconducting undulator 1 m from the dipole. An optical "trombone" delay line will provide the large shift in focus. We discuss the optical design, diffraction, depth of field, and the expected signals over the energy ramp, for emission from the centre and edge of the dipole and from the undulator.

INTRODUCTION

The two LHC synchrotron-light telescopes (BRST [1]) will measure the transverse beam profiles. The abort-gap monitor (AGM or BRSA [2]) will verify that the 3-μs gap contains an acceptably small number of particles, since a partial kick during the rise of the abort kicker may drive them into a magnet and cause a quench.

Protons will be injected at 450 GeV and ramped to collisions at 7-TeV, where they emit enough synchrotron light in superconducting dipoles for imaging. However, arc dipoles are interconnected in a long series of cryostats, with no access to this light. In the IR-4 straight, a chicane of four 9.45-m dipoles widens the beam separation from 194 to 420 mm for RF cavities. As the beam exits the cavities, dipole D3 bends it by 1.57 mrad. In the 62-m drift to the fourth dipole, light from the first 3 m of D3 diverges from the protons, reflects from an extraction mirror at 26 m, and passes through a fused-silica vacuum viewport to optics below the beamline. The dipoles ramp to 3.88 T at 7 TeV, bringing the critical wavelength λ_c from 0.23 mm to 61 nm in an orbit with radius ρ=6 km.

At injection, since the dipole's visible emission is negligible, a short superconducting undulator [3] with N_u=2 periods of λ_u=28 cm was added to the cryostat 937 mm before D3. With B_u=5 T (not ramped), its spectrum for 450-GeV protons peaks in the visible, at 610 nm.

The ALICE detector will study lead-ion rather than proton collisions. With fewer particles and a red-shifted spectrum, this experiment requires separate evaluation.

Since ρ must be the same for proton and ion orbits, at a given dipole field the energy must scale with charge. Lead ions will collide at Z=82 times the 7-TeV proton energy (92 μJ/ion!). The relativistic factor γ scales by Z/A.

EMITTED ENERGY PER PARTICLE

For central dipole radiation, the energy per particle emitted (in both polarizations) into solid angle and frequency $d\xi d\psi d\omega$ (where the horizontal and vertical angles ξ/γ and ψ/γ are conveniently expressed in normalized form) is expressed using modified Bessel functions K [4]:

$$W_d = Z^2 \frac{3}{4\pi^2} W_0 \left(\frac{\omega}{\omega_c}\right)^2 \left(1+\psi^2\right)^2 \left[K_{2/3}^2(\zeta) + \frac{\psi^2}{1+\psi^2} K_{1/3}^2(\zeta)\right] \tag{1}$$

$$W_0 = \frac{e^2}{4\pi\varepsilon_0 c} = 7.6956 \cdot 10^{-37}\ \mathrm{J \cdot s} \tag{2}$$

$$\zeta = \frac{\omega}{2\omega_c}\left(1+\psi^2\right)^{3/2} \tag{3}$$

$$\omega_c = \frac{2\pi c}{\lambda_c} = \frac{3}{2}\gamma^3 \frac{c}{\rho} \tag{4}$$

We model the dipole's edge field as:

$$B(z) = \frac{B_d}{2}\left(1 + \frac{2}{\pi}\arctan\frac{z}{L_e}\right) \tag{5}$$

The edge radiation is then given by [5]:

$$W_e = Z^2 \frac{8}{9\pi^2} W_0 \left(\frac{\omega_c}{\omega}\right)^2 \frac{\left(1-\xi^2+\psi^2\right)^2 + \left(2\xi\psi\right)^2}{\left(1+\xi^2+\psi^2\right)^6} \cdot \exp\left[-\frac{\omega L_e}{\gamma^2 c}\left(1+\xi^2+\psi^2\right)\right] \tag{6}$$

Note that this expression diverges for $\omega << \omega_c$; these low frequencies are emitted as the particle moves from the edge to the uniform field, and so edge and central radiation are not really distinct in this range.

The energy from undulator radiation is given by [4]:

$$W_u = \frac{Z^4}{A^2} N_u^2 K_u^2 W_0 \frac{\left(1-\xi^2+\psi^2\right)^2 + \left(2\xi\psi\right)^2}{\left(1+\xi^2+\psi^2\right)^4} \cdot \left(\frac{2\omega}{\omega+\omega_1}\right)^2 \mathrm{sinc}^2\left(\pi N_u \frac{\omega-\omega_1}{\omega_1}\right) \tag{7}$$

with undulator parameter K_u and first-harmonic ω_1:

$$K_u = \frac{eB_u\lambda_u}{2\pi m_p c} \tag{8}$$

$$\omega_1 = \frac{4\pi\gamma^2 c}{\lambda_u\left(1+\xi^2+\psi^2\right)} \tag{9}$$

OPTICAL CONSIDERATIONS

Depth of Field in the Dipole

Due to the small bend angle, dipole light will be collected over a long path. In the horizontal plane, rays are emitted tangent to the orbit (Fig. 1). They focus in the optical system as if originating at their intersection R with the focal plane. We see which ray angles from a point M

*afisher@slac.stanford.edu

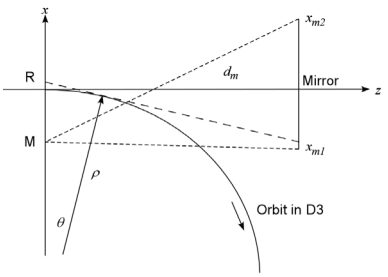

Figure 1: Radiation from a point inside the dipole.

on the focal plane intersect the extraction mirror. Fig. 2(a) plots these positions and angles in phase space. We see that the mirror reflects light from the first 3.2 m of the orbit in D3. The plot also shows the acceptance of a slit placed one focal length after the first focusing optic, in order to select a range of angles from the source plane. The focus is set in the middle of the path determined by the slit.

The beam ellipses from different points along the orbit project onto the x axis with small shifts, but the shifts are minimized by focusing in the middle. A sum of the projections along the entire selected path confirms that the broadening is <2% for the full 3 m accepted here.

In vertical phase space (Fig. 2(b)), the large radiation opening angle makes wide radiation phase ellipses that remain centered (since the orbit is straight) but rotate with distance in the dipole, widening the sum of projections. Blurring is again reduced by focusing in the middle of the path, but it becomes a problem for paths over 2 m.

Diffraction

A wide angular spread is needed for a small optical waist and hence for good size resolution. For a given angular width, the TEM_{00} mode has the smallest waist and so offers a lower bound on resolution. A TEM_{00} beam at 400 nm with an RMS size of 330 µm, typical of a beam in D3, has an RMS angular spread of 100 µrad. The vertical angle of dipole radiation from 7-TeV protons is wider, 182 µrad, and a 2-m path gives a (uniform) horizontal spread of 324 µrad. A ZEMAX [6] calculation at 400 nm finds an overall broadening of 5%. Ions, with a smaller γ and so larger angles, give less concern.

Optical System

To match the wide spectrum over the ramp, we focus with two metal-coated mirrors. A crowded rail under the beamline is being replaced by an optical table, allowing space for calibration and focusing (Fig. 3). The first mirror, F1, is 32 m from the source; to form its image on the table, it must demagnify. The second mirror, F2, raises the overall magnification to 0.3, so that the image covers multiple camera pixels. With incidence at 1° to the normal on both spherical mirrors, ZEMAX finds an RMS point spread on the image of 16 µm from aberration.

A design improving on spherical optics was developed. Since any portion of the surface of an ellipse has perfect geometric point-to-point imaging, elliptical mirrors can be devised for any angle of incidence. Indeed, the spot size remains below 1 µm RMS even with source points 1 mm off axis and with the window's slight chromaticity. However, such mirrors are costly, and the geometric blurring from spherical optics is less of a concern than diffraction. Elliptical optics may be useful as an upgrade.

Since the light source shifts by up to 2.8 m during the ramp, from the undulator's centre to 1.6 m inside D3, the optical focus must change. Moving focusing mirrors while maintaining focus and alignment is difficult. Instead, the entering optical path is held constant by an optical "trombone" (Fig. 3). A 2-pass trombone using a 600-mm motorized translation stage can delay by 1200 mm. For up to 3 m, needed to focus in the dipole, a second stage inserts two mirrors into the path on the moving platform, making a 4-pass trombone.

SIGNALS ON THE DETECTORS

Camera

An image-intensified camera (Proxicam HL4 S NIR with a red-enhanced S25 photocathode) replaces a CCD. Combining (1), (6), and (7) with the spectral responses of the camera (300 to 900 nm), the metal-coated mirrors (>380 nm for protected silver) and the viewport (<4 µm, with an opaque notch around 2.8 µm), gives the number of electrons emitted from the photocathode.

Fig. 4 shows the signals in the peak pixel for the expected beam size and the fills of Table 1. The intensifier can brighten these signals, but cannot improve the signal-to-noise ratio from the square root of this photoelectron count. The drop in in-band undulator radiation before the dipole radiation rises causes a crossover region with a deep dip in available light plus blurring from multiple sources. Manipulating the focal-plane slit helps to speed this transition from undulator to dipole.

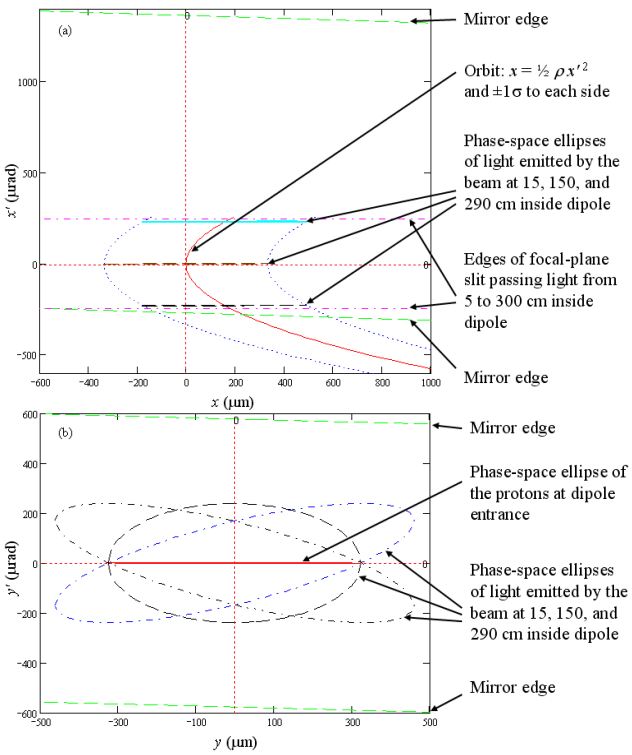

Figure 2: (a) Horizontal and (b) vertical phase space for emission in D3, with the coordinates and the optical focus in middle of the path selected by the slit.

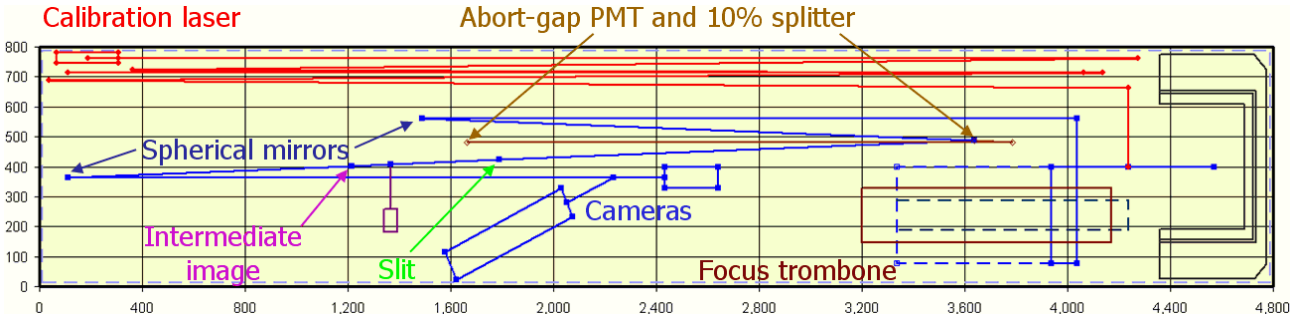

Figure 3: A new 4.8×0.8 m^2 optical table below the beam adds a calibration path and focus trombone. Light enters at right.

At injection, a proton pilot bunch needs an integration time of at least 1 s. For lead ions, there is simply too little light in the visible to see an injected pilot bunch, but with sufficient integration, a full bunch might be imaged. This limitation is lifted once the ramp begins, shifting undulator light out of the infrared.

Abort-Gap Monitor

A beamsplitter between F1 and F2 (Fig. 3) reflects 90% of the light (before cutting by the slit) for imaging and transmits 10% to the AGM. A photomultiplier (PMT) is placed on the split path at the intermediate image from F1, where the light fits easily into the 10-mm photocathode. The gated PMT (Hamamatsu R5916-50) uses a microchannel plate rather than dynodes. The gate allows it to sensitively detect the small gap signal without saturation from the large population elsewhere.

The 3-μs gap is monitored in 30 100-ns bins. The beam-loss monitor group has calculated the proton population per bin at quench threshold [7]. Jowett explains [8] that ions fragment hitting the beam screen and deposit the same energy in a magnet coil as Z protons at the corresponding stage of the ramp. We thus set the threshold at $1/Z$ times the quench limit for protons.

The calculated PMT signals meet the requirement to measure a threshold population to 5% accuracy in 100 ms throughout the ramp—except for lead ions at injection. Since this case is difficult for imaging too, all the light should then be sent to the PMT. This factor of 10 provides sufficient improvement to meet the criterion.

Table 1: Proton and lead-ion fills

	Protons	**Ions**
Number per pilot bunch	5×10^{9}	7×10^{7}
Number per full bunch	1.7×10^{11}	8.2×10^{9}
Number of bunches, full ring	2808	592

REFERENCES

[1] L. Ponce, R. Jung and F. Méot, "LHC Proton Beam Diagnostics Using Synchrotron Radiation", CERN-2004-007.

[2] C. Fischer, "High Sensitivity Measurement of the Longitudinal Distribution of the LHC Beams", LHC-B-ES-0005.00 rev. 2.0.

[3] R. Maccaferri, M. Facchini, R. Jung, D. Tommasini and W. Venturini Delsolaro, "The 5-T Superconducting Undulator for the LHC Synchrotron Radiation Profile Monitor", LHC Project Report 731, EPAC, 5-9 July 2004, Lucerne, Switzerland.

[4] Albert Hofmann, *The Physics of Synchrotron Radiation*, Cambridge University Press, (2004).

[5] R. Coïsson, "Angular-Spectral Distribution and Polarization of Synchrotron Radiation from a 'Short' Magnet", Phys. Rev. A **20** (1979), pp. 524-528.

[6] ZEMAX Development Corp., http://www.zemax.com

[7] B. Dehning and M. Sapinski, private communication.

[8] J.M. Jowett, "Ions in the LHC", CERN, Chamonix Workshop, 2009.

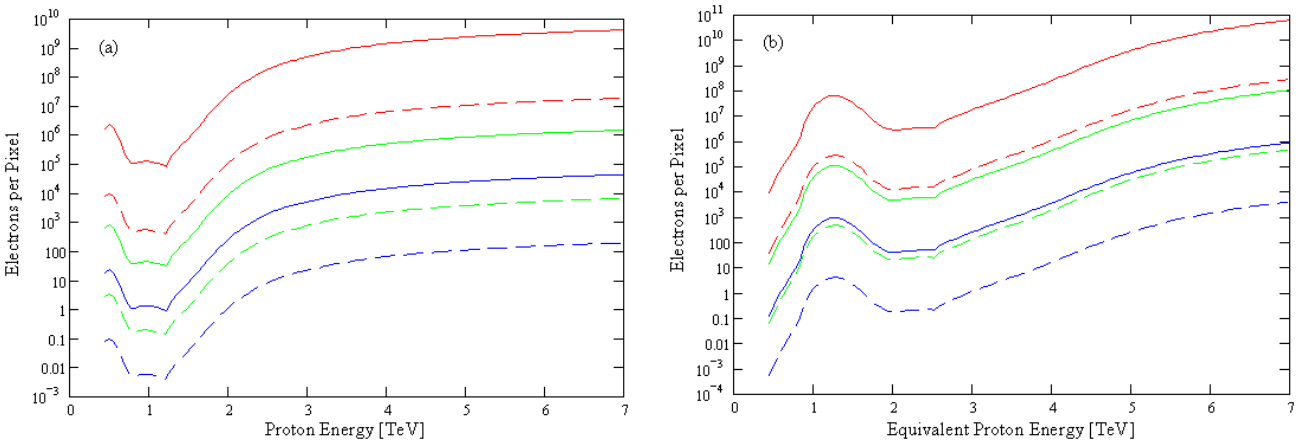

Figure 4: Electrons in the peak pixel of the camera in one turn (dashed curves) and in a 20-ms video interval (solid curves); for a pilot bunch (blue), a single full bunch (green), and a full ring (red). (a) Protons and (b) lead ions.